Available online at www.sciencedirect.com

ScienceDirect

Advances in Space Research 52 (2013) 2015–2033

ADVANCES IN SPACE RESEARCH (a COSPAR publication)

www.elsevier.com/locate/asr

Assimilation of endmember variability in spectral mixture analysis for urban land cover extraction

Uttam Kumar [a,b,c], S. Kumar Raja [d], Chiranjit Mukhopadhyay [b], T.V. Ramachandra [a,e,f,*]

[a] Energy & Wetlands Research Group, Centre for Ecological Sciences, Indian Institute of Science, Bangalore 560012, India
[b] Department of Management Studies, Indian Institute of Science, Bangalore 560012, India
[c] International Institute of Information Technology (IIITB), Bangalore 560100, India
[d] EADS Innovation Works, Airbus Engineering Centre India, Xylem No. 4, Mahadevapura Post, Whitefield Road, Bangalore 560048, India
[e] Centre for Sustainable Technologies, Indian Institute of Science, Bangalore 560012, India
[f] Centre for Infrastructure, Sustainable Transportation and Urban Planning, Indian Institute of Science, Bangalore 560012, India

Received 16 July 2012; received in revised form 3 August 2013; accepted 16 August 2013
Available online 30 August 2013

Abstract

Variable Endmember Constrained Least Square (VECLS) technique is proposed to account endmember variability in the linear mixture model by incorporating the variance for each class, the signals of which varies from pixel to pixel due to change in urban land cover (LC) structures. VECLS is first tested with a computer simulated three class endmember considering four bands having small, medium and large variability with three different spatial resolutions. The technique is next validated with real datasets of IKONOS, Landsat ETM+ and MODIS. The results show that correlation between actual and estimated proportion is higher by an average of 0.25 for the artificial datasets compared to a situation where variability is not considered. With IKONOS, Landsat ETM+ and MODIS data, the average correlation increased by 0.15 for 2 and 3 classes and by 0.19 for 4 classes, when compared to single endmember per class.

Keywords: Linear mixture model; Mixed pixel; Variable endmember

1. Introduction

Urban areas are currently among the most rapidly changing land cover (LC) types on the Earth. Urban cities are the loci of human population and activities, and are therefore sites of significant natural resource transformation (Lambin et al., 2001). Remote sensing (RS) has been widely used to provide a timely and synoptic view of urban LC (Kumar et al., 2011b; Yang and Lo, 2002). More often than not, the accuracy of urban LC mapping is limited by the presence of mixed pixels (Kumar et al., 2008). Deriving accurate, quantitative measures over urban area remains a fundamental research challenge due to the great spatial and spectral variability of the materials (Forster, 1985; Lu and Weng, 2004; Xian and Crane, 2005). In highly variable scenes, spatial heterogeneity (in the types and conditions) of endmembers of urban surface materials is problematic at multiple spatial scales, resulting in a high percentage of mixed pixels in most moderate to low spatial resolution imagery and occasionally, even limiting the utility of high spatial resolution imagery (Myint et al., 2004; Small, 2005; Somers et al., 2011).

There are two principal approaches to retrieve information on LC from multispectral (MS) satellite images. The most common approach to characterise LC from RS data is hard classification; assigning all pixels in the image to

* Corresponding author at: Energy & Wetlands Research Group, Centre for Ecological Sciences, Indian Institute of Science, Bangalore 560012, India.
E-mail addresses: uttam@ces.iisc.ernet.in (U. Kumar), sk.kumar.raja@gmail.com (S.K. Raja), cm@mgmt.iisc.ernet.in (C. Mukhopadhyay), cestvr@ces.iisc.ernet.in (T.V. Ramachandra).
URLs: http://ces.iisc.ernet.in/energy, http://ces.iisc.ernet.in/foss (T.V. Ramachandra).

0273-1177/$36.00
http://dx.doi.org/10.1016/j.asr.2013.08.022

mutually exclusive classes such as built-up, water, vegetation, etc. (Carlson and Sanchez-Azofeifa, 1999; Kumar et al., 2011c; Powell et al., 2007) generating a thematic map at the resolution of the bands. This approach is problematic for several reasons – firstly, most urban LC classes are not spectrally distinct resulting in considerable confusion between classes (Small, 2005). Secondly, physical composition of the classes may vary due to different building materials and different construction practices and therefore cross regional comparisons between urban areas are limited (Small, 2005). This method depends on the assumption that two signals corresponding to one cover type are much more similar to each other than the two signals from different cover types (Settle, 2006). Another approach is linear unmixing – the linear mixture model (LMM), which allows a number of different LC types to be present, each contributing a fraction of its (unique, fixed) spectrum where fraction corresponds to the area occupied by that LC type which is obtained by inverting the model to produce estimates of those fractional abundances. The spectral signature (endmember) for each class may be obtained from the image itself (Bateson et al., 2000; Boardman, 1995; Kumar et al., 2008, 2012; Plaza et al., 2004; Settle, 2006; Winter and Winter, 2000) or from libraries of reference spectra (Dennison and Roberts, 2003). The selection of endmembers involves identifying both the number and type of endmembers and their corresponding spectral signatures. Various approaches for selecting endmembers have been proposed (refer Plaza et al., 2004, 2005; Martinez et al., 2006; Miao and Qi, 2007; Dobigeon et al., 2009, etc.). However, the use of fixed endmember spectra does not take into account the variation in endmember spectral signatures caused by differential illumination conditions, spatial and temporal variability in the scene components resulting in significant fraction estimate errors.

The pixel-to-pixel variability in an image can be explained in two different ways as described by Settle (2006). Firstly, the main distinction is between pixels of different LC types, with further variation coming from within-class variability. Secondly, there is no within-class variability, but the variations in reflectance within the pixels arise from pixel-to-pixel variations in the fractional coverage. This could lead us to infer that if the intrinsic scale of the pixel is smaller than the changes in LC type, hard classification is justified, while unmixing is appropriate when the case is reverse, given the underlying class membership model. The fundamental reason for this variability is the issue of scale and hence toggling between the two models for addressing the variability in surface reflectance may not be appropriate. The phenomenon of variability is prevalent at a fine scale and it is unreasonable to ignore the effect of variability in pure LC classes at sufficiently high resolution while observing the same at a moderate or coarse resolution (Settle, 2006). Standard LMM assumes a fixed number of representative endmembers and the entire image is modeled in terms of those spectral components. However, urban environments are particularly difficult to model because a single endmember cannot account for considerable spectral variation within a class as they exhibit high degrees of spectral heterogeneity on fine scales. The procedure is limited because the selected endmember spectra may not effectively model all the elements in the image, or a pixel may be modeled by endmembers that do not actually correspond to the materials located in its field of view and result in decreased accuracy of the estimated fractions (Sabol et al., 1992). Thus, for each pixel, it may sometimes be more appropriate to recognise that a distribution of possible coverage may be derived for each class. The width of this distribution is a function of the degree of intra-class spectral variation (variability within the endmember class) present and will impact on the use of the sub-pixel classification output.

Various attempts have been made to address endmember variability. Somers et al. (2011) presented a detailed review of the available methods and results of endmember variability reduction in spectral mixture analysis based on the hypothesized five principles which are reviewed at the end of Section 3 (after the conceptual framework of VEC-LS algorithm). In recent times, numerous solutions (Somers et al., 2010a,b) to account endmember variability have been proposed including the hierarchical Multiple Endmember Spectral Mixture Analysis (MESMA, Roberts et al., 1998) applied to map urban LC in Bonn, Germany, with a Hymap (126 spectral bands) and 4 levels of classification using 1521 endmembers obtained using EAR, MASA and COB (Franke et al., 2009). MESMA was also applied on Landsat ETM+ with four endmembers (vegetation, impervious surface, soil and water) for Manaus, Brazil (Powell et al., 2007). Foody and Doan (2007) reported the impact of intra-class spectral variability on the estimation of sub-pixel LC class composition concluding that class variation has an impact on the accuracy of sub-pixel class composition estimation, as it violates the assumption that a class can be represented by a single endmember. Settle (2006) attempted to derive an improved representation of error term in the mixture model, taking account of the variability of the endmember spectra and of sub-pixel variation in fraction abundance of surface cover. Song (2005) proposed a Bayesian spectral mixture analysis (BSMA) model to understand the impact of endmember variability on the deviation of sub-pixel vegetation fractions in an urban environment. This approach is similar to iterative mixture analysis, i.e., each pixel is unmixed with randomly selected combinations of endmember signatures, represented by probability density functions. BSMA accounts the probabilities of spectral signatures instead of assuming equal probabilities for all endmembers. Bateson et al., (2000) constructed endmember bundles to produce minimum and maximum fraction images bounding the correct cover fractions and specifying error due to endmember variability. Recently, a pre-screened and normalised MESMA which includes a new endmember selection strategy and an integration of the normalised spectral mixture analysis (NSMA) and MESMA for estimating impervious surface

area fraction was proposed by Yang et al., (2010). The methods proposed above are different in their approaches, underlying principles and assumptions. They have been tested on different datasets and there is no proper guideline as to which method and spatial resolution would be most suitable for optical RS data for a regional level urban area classification while taking into account the intra and inter class variability, i.e., similarity among endmember classes (Zhang et al., 2006).

Here, we propose a novel technique – *variable endmember constrained least square* (VECLS) for addressing the endmember variability in an image. The methodology for classification allows the signals within a class to vary from pixel to pixel about a mean spectrum. Each class is then represented by the mean and by a variance-covariance matrix that captures the statistical variability around the mean, and allocation decisions are based on a modified form of statistical pattern matching. Many instances of a particular endmember are chosen from the image to take into account its variability. This inter-class variance is accounted by constructing a covariance matrix that varies around the selected endmember mean. The algorithm is first applied on a computer simulated dataset with 4 bands and 3 classes having small, medium and large variability in the endmember's spread. The technique is then tested on real datasets acquired from IKONOS, Landsat ETM+ and MODIS sensors taking 2, 3 and 4 classes. The method is compared with a situation when there are no variances in the endmembers, i.e., covariance within an endmember is zero. The results are validated with a high resolution classified map using correlation, root mean square error (RMSE), and bidirectional function (BDF) plots. The overall methodology is as depicted in Fig. 1.

The paper is organised as follows. Section 2 discusses the general linear model and the framework for VECLS algorithm is described in Section 3. Section 4 presents data and methods, followed by results and discussion in Section 5 and 6 respectively, with concluding remarks in Section 7.

2. Linear model

Linear unmixing assumes that a satellite signal is modeled as a weighted sum of a limited number of basic signals, where each of these signals is characteristic of one of a number of LC types contributing to the signal. If there are M spectral bands and N classes, then associated with each pixel is a M-dimensional vector $\mathbf{y}$ whose components are the gray values corresponding to the M bands. Let $\mathbf{E} = [e_1, \ldots, e_{n-1}, e_n, e_{n+1}, \ldots, e_N]$ be a $M \times N$ matrix, where $\{e_n\}$ is a column vector representing the spectral signature (endmember) of the nth target material. For a given pixel, the abundance or fraction of the nth target material present in a pixel is denoted by α_n, and these values are the components of the N-dimensional abundance vector $\boldsymbol{\alpha}$. Assuming LMM (Shimabukuro and Smith, 1991), the observation vector $\mathbf{y}$ is related to $\mathbf{E}$ by

$$\mathbf{y} = \mathbf{E}\boldsymbol{\alpha} + \boldsymbol{\eta} \tag{1}$$

where $\boldsymbol{\eta}$ accounts for the measurement noise. We further assume that the components of the noise vector $\boldsymbol{\eta}$ are zero-mean random variables that are i.i.d. (independent and identically distributed). Therefore, the covariance matrix of the noise vector is $\sigma^2\mathbf{I}$, where σ^2 is the variance, and $\mathbf{I}$ is $M \times M$ identity matrix. Two constraints imposed on the abundances in Eq. (1) are the non-negativity and sum-to-one given as

$$\alpha_n \geqslant 0, \forall n : 1 \leqslant n \leqslant N \tag{2}$$

and

$$\sum_{n=1}^{N} \alpha_n = 1 \tag{3}$$

This allows proportions of each pixel to be partitioned between classes. The conventional approach (Nielsen, 2001) to extract the abundance values is to minimise $||\mathbf{y} - \mathbf{E}\boldsymbol{\alpha}||$, and the Unconstrained Least Squares estimate for the abundance is

$$\boldsymbol{\alpha} = (\mathbf{E}^T\mathbf{E})^{-1}\mathbf{E}^T\mathbf{y} \tag{4}$$

Imposing the unity constraint on the abundance values while minimising $||\mathbf{y} - \mathbf{E}\boldsymbol{\alpha}||$, gives the Constrained Least Squares (CLS) estimate of the abundance as,

$$\boldsymbol{\alpha} = (\mathbf{E}^T\mathbf{E})^{-1}(\mathbf{E}^T\mathbf{y} - \frac{\lambda}{2}1) \tag{5}$$

where

$$\lambda = \frac{2(1^T(\mathbf{E}^T\mathbf{E})^{-1}\mathbf{E}^T\mathbf{y} - 1)}{1^T(E^TE)^{-1}1} \tag{6}$$

3. Conceptual framework for Variable Endmember Constrained Least Square (VECLS)

Intra-class variability of remotely sensed data is often too high or too low for unmixing a single pixel (Petrou and Foschi, 1999). In such situations, the endmember of a particular class are not strictly unique vectors and there is always a variation within that class. Therefore, we modify Eq. (1) to represent variable endmembers as random vectors, and introduce the following statistical LMM

$$\underset{\sim}{y} = \sum_{n=1}^{N} \underset{\sim}{e_n}\ \underset{\sim}{\alpha_n} \tag{7}$$

where, $\{\alpha_n\}$ is the observed set of M reflectance values and $\underset{\sim}{e}$ is the random vector representing the variable endmember of class n. The endmembers of each class n are drawn from a probability distribution defined by the probability density function (p.d.f.) $f_n(\underset{\sim}{e_n})$. It is reasonable to make an assumption that endmember p.d.f.s of distinct LC categories are mutually independent. For example, the spectral signature distribution of builtup and vegetation can be

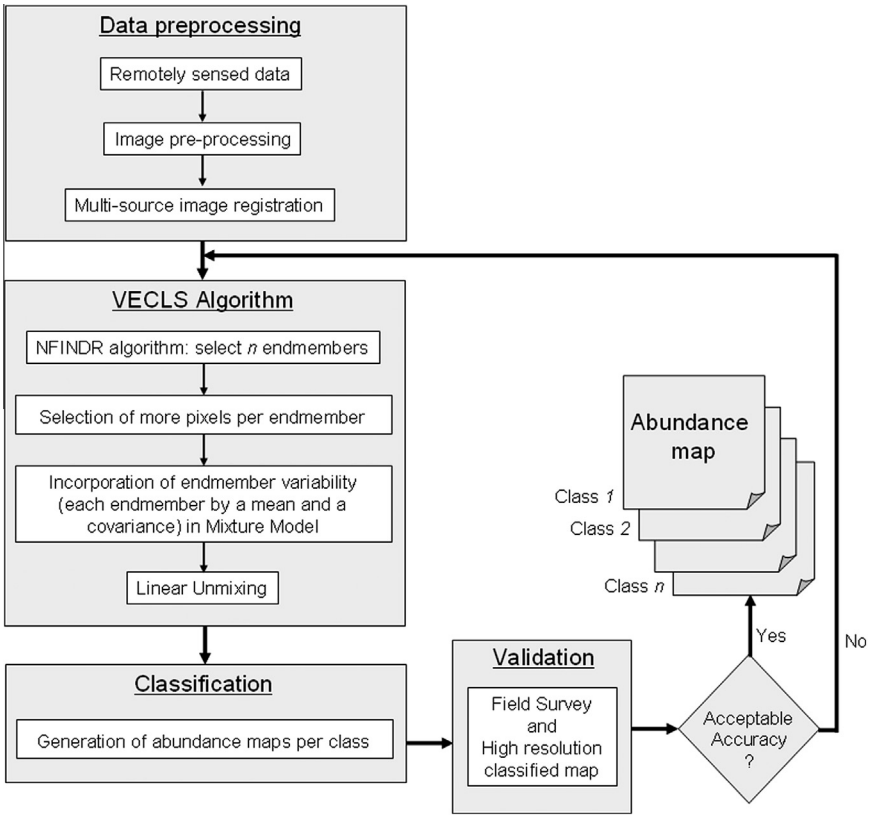

Fig. 1. Flow chart outlining methods.

treated independently. As a consequence of the above assumption, $\{e_n \alpha_n\}$ are also mutually independent. If we denote $e_n \alpha_n$ as y_n, Eq. (7) can be rewritten as

$$y = \sum_{n=1}^{N} y_n \tag{8}$$

and p.d.f. of y_n can be shown to be $\frac{1}{\alpha_n^m} f_n(\frac{y_n}{\alpha_n})$. Since $\{y_n\}$ are mutually independent, p.d.f. of $\{y\}$ is given by

$$p_y(\mathbf{y}) = \left[\frac{1}{\alpha_1^M} f_1\left(\frac{\mathbf{y}_1}{\alpha_1}\right)\right] * \left[\frac{1}{\alpha_2^M} f_1\left(\frac{\mathbf{y}_2}{\alpha_2}\right)\right] * \cdots * \left[\frac{1}{\alpha_m^M} f_1\left(\frac{\mathbf{y}_m}{\alpha_m}\right)\right], \tag{9}$$

where $*$ denotes a convolution operator. Note that p.d.f. of $\{y\}$ implicitly depends on the abundance values $\{\alpha_n\}$. Given the observation vector $\mathbf{y}$, we define the *likelihood function* L as

$$L(\alpha_1, \ldots, \alpha_{n-1}, \alpha_n, \alpha_{n+1}, \ldots, \alpha_N) = p_y(\mathbf{y}; \alpha_1, \ldots, \alpha_{n-1}, \alpha_n, \alpha_{n+1} \ldots, \alpha_N) \tag{10}$$

Here, we estimate abundance values by seeking $\{\alpha_n\}$ which maximises the likelihood function subject to the constraint that sum of all abundance values add to 1, which is the value of $\{\alpha_n\}$ that maximises the likelihood function. This means, given $\alpha_1, \ldots, \alpha_{n-1}, \alpha_n, \alpha_{n+1}, \ldots, \alpha_N$, α_n is the value for which y has the maximum chance to occur. Also note that abundance values are deterministic quantities.

We first assume a Gaussian case and then subsequently move on to a generalised case, where the form of p.d.f. is not assumed. Let μ_n and C_n be mean vector and covariance of nth target material, respectively. It is clear from LMM in Eq. (7) that the distribution of observation (y) is also Gaussian whose mean and covariance are given by

$$\boldsymbol{\mu} = \sum_{n=1}^{N} \alpha_n \mu_n, \mathbf{C} = \sum_{n=1}^{N} \alpha_n^2 C_n \tag{11}$$

In our framework, in order to find the ML (Maximum Likelihood) abundances, we maximise the log-likelihood

$$L(\alpha_1, \ldots, \alpha_{n-1}, \alpha_n, \alpha_{n+1}, \ldots, \alpha_N; \mathbf{y}) = -\frac{1}{2}\log(\det[C]) - \frac{1}{2}(\mathbf{y} - \mu)^T \mathbf{C}^{-1}(\mathbf{y} - \mu) \tag{12}$$

The above approach is based on the assumption that the underlying distribution of the spectral signatures are normal.

Next, in what follows we show a framework where no assumption on the form of p.d.f. is made. Let $\mathbf{Z}$ be a matrix whose column are the means of the spectral signatures, i.e., $\mathbf{Z} = [\mu_1, \ldots, \mu_{n-1}, \mu_n, \mu_{n+1}, \ldots, \mu_N]$. Suppose that the actual observation is $\mathbf{o}$, then we seek to minimise the deviation

between $\mathbf{o}$ and $\underset{\sim}{y}$ subject to constraints given in Eq. (3). We minimise,

$$F(\boldsymbol{\alpha},\lambda)=E\left\{\left(\mathbf{o}-\sum_{n=1}^{N}\underset{\sim}{e_n}\,\underset{\sim}{\alpha_n}\right)^{T}\left(\mathbf{o}-\sum_{n=1}^{N}\underset{\sim}{e_n}\,\underset{\sim}{\alpha_n}\right)\right\}+\lambda\left(\sum_{n=1}^{N}\underset{\sim}{\alpha_m}-\mathbf{1}\right) \tag{13}$$

where $E\{.\}$ is the expectation operator and λ is the Lagrangian multiplier for enforcing the constraint on the abundance. Using (11), it is easy to simplify the expectation term in expression (13) as follows:

$$=E\left\{\left(\mathbf{o}-\boldsymbol{\mu}+\boldsymbol{\mu}-\sum_{n=1}^{n}\underset{\sim}{\alpha_n}\,\underset{\sim}{y_n}\right)^{T}+\left(\mathbf{o}-\boldsymbol{\mu}+\boldsymbol{\mu}-\sum_{n=1}^{n}\underset{\sim}{\alpha_n}\,\underset{\sim}{y_n}\right)\right\} \tag{14}$$

$$=E\{(\mathbf{o}-\boldsymbol{\mu})^{T}(\mathbf{o}-\boldsymbol{\mu})\}+E\left\{\left(\boldsymbol{\mu}-\sum_{n=1}^{N}\underset{\sim}{\alpha_n}\,\underset{\sim}{y_n}\right)^{T}\left(\boldsymbol{\mu}-\sum_{n=1}^{N}\underset{\sim}{\alpha_n}\,\underset{\sim}{y_n}\right)\right\} \tag{15}$$

$$=(\mathbf{o}-\boldsymbol{\mu})^{T}(\mathbf{o}-\boldsymbol{\mu})+\sum_{n=1}^{N}\underset{\sim}{\alpha_n^2}\,Trace[C_n] \tag{16}$$

Note that in Eq. (16) no cross-correlation terms appear. Denoting $\mathbf{V}$ as the diagonal matrix whose nth diagonal element is the trace of C_n (covariance of nth target material), the objective function F($\boldsymbol{\alpha}$) can be written in a more compact form using $\mathbf{Z}$ and $\mathbf{V}$ as

$$F(\boldsymbol{\alpha},\lambda)=(\mathbf{o}-\mathbf{Z}_{\alpha})^{T}(\mathbf{o}-\mathbf{Z}_{\alpha})+\boldsymbol{\alpha}^{T}V\boldsymbol{\alpha}+\lambda(\boldsymbol{\alpha}^{T}\mathbf{1}-\mathbf{1}) \tag{17}$$

where $\mathbf{1}$ is a vector whose components are all 1. In order to find the minima, we first take the first derivative of F(α) with respect to $\{\alpha_n\}$, λ and equate it to 0.

$$\frac{\partial F(\boldsymbol{\alpha},\lambda)}{\partial\boldsymbol{\alpha}}=2\mathbf{Z}^{T}\mathbf{Z}\boldsymbol{\alpha}-2\mathbf{Z}^{T}\mathbf{o}+2\mathbf{V}\boldsymbol{\alpha}+\lambda\mathbf{1}=0 \tag{18}$$

$$\frac{\partial F(\boldsymbol{\alpha},\lambda)}{\partial\lambda}=\boldsymbol{\alpha}^{T}\mathbf{1}-\mathbf{1}=0 \tag{19}$$

$$2\mathbf{Z}^{T}\mathbf{Z}\boldsymbol{\alpha}-2\mathbf{Z}^{T}\mathbf{o}+2\mathbf{V}\boldsymbol{\alpha}+\lambda\mathbf{1}=0$$

$$\boldsymbol{\alpha}=\frac{2\mathbf{Z}^{T}\mathbf{o}-\lambda\mathbf{1}}{2\mathbf{Z}^{T}\mathbf{Z}+2\mathbf{V}}=\frac{\mathbf{Z}^{T}\mathbf{o}-\frac{\lambda}{2}\mathbf{1}}{\mathbf{Z}^{T}\mathbf{Z}+\mathbf{V}} \tag{20}$$

$$\boxed{\boldsymbol{\alpha}=\left(\mathbf{Z}^{T}\mathbf{Z}+\mathbf{V}\right)^{-1}\left(\mathbf{Z}^{T}\mathbf{o}-\tfrac{\lambda}{2}1\right)} \tag{21}$$

Now we derive an explicit expression for λ. Denoting $\boldsymbol{\alpha}_0=(\mathbf{Z}^{T}\mathbf{Z}+\mathbf{V})^{-1}\mathbf{Z}^{T}\mathbf{o}$, Eq. (20) can be written as

$$\boldsymbol{\alpha}_0=\boldsymbol{\alpha}_0-\frac{\lambda}{2}(\mathbf{Z}^{T}\mathbf{Z}+\mathbf{V})^{-1}\mathbf{1} \tag{22}$$

Multiplying $\mathbf{1}^{\mathrm{T}}$ on both sides, we get

$$\mathbf{1}^{T}\boldsymbol{\alpha}=\mathbf{1}^{T}\boldsymbol{\alpha}_0-\frac{\lambda\mathbf{1}^{T}(\mathbf{Z}^{T}\mathbf{Z}+\mathbf{V})^{-1}1}{2} \tag{23}$$

Note that $1^{\mathrm{T}}\alpha=1$. Therefore the final expression for λ is

$$\mathbf{1}^{T}\boldsymbol{\alpha}_0=\frac{\lambda}{2}\mathbf{1}^{T}(\mathbf{Z}^{T}\mathbf{Z}+\mathbf{V})^{-1}\mathbf{1} \tag{24}$$

$$\boxed{\lambda=\frac{2(\alpha_0^{T}1-1)}{1^{T}(Z^{T}Z+V)^{-1}1}} \tag{25}$$

In conventional approach, where the endmembers are assumed to be constant, $\mathbf{Z}$ represents the endmember matrix ($\mathbf{V}=0$), and the endmembers are obtained by minimising

$$(\mathbf{o}-\mathbf{Z}\boldsymbol{\alpha})^{T}(\mathbf{o}-\mathrm{Z}\alpha)+\lambda(\boldsymbol{\alpha}^{T}\mathbf{1}-\mathbf{1}) \tag{26}$$

subject to the constraint that $\boldsymbol{\alpha}^{T}\mathbf{1}=1$. However, in this approach, we have assumed the endmembers to be variable, and as a consequence the endmember variability term namely $\mathbf{V}$ has been accounted.

The spectral mixture analysis (SMA) techniques for addressing endmember variability have been broadly categorised (Somers et al., 2011) based on five basic principles: (i) iterative mixture analysis cycle, (ii) spectral feature selection, (iii) spectral weighting, (iv) spectral transformations, and (v) spectral modelling. Table 1 compares VECLS with the existing techniques (Somers et al., 2011) and it is evident that VECLS is conceptually different as VECLS is not iterative, does not involve spectral feature selection, spectral weighting, spectral transformation or even spectral modelling. Hence VECLS has been placed as a separate category in the table for comparison. The underlying genesis behind the methods, advantages and disadvantages are also highlighted.

4. Data and methods

A major problem involved in analysing the quality of fractional estimation methods is the fact that ground truth information about the real abundances of materials at sub-pixel levels is difficult to obtain in real scenarios. Therefore, simulated dataset were used to illustrate and explore the effect of class spectral variability on sub-pixel class composition estimation in a controlled analysis as single class is difficult to be adequately represented by a unique endmember which remains an implicit assumption in unmixing (Asner, 1998; Song and Woodcock, 2003; Townshend et al., 1992). Advantages are that the exact endmember fractions are known and in addition, the non-linear interactions of photons among endmembers (Kumar et al., 2012) do not exist, simplifying the problem and allowing better understanding of the impact of endmember variability.

With real time RS data, the impacts of class spectral variation on sub-pixel class composition estimation has been illustrated by addressing the spatial variability of LC components as a combination of endmembers, and spectral variability has been addressed by allowing the number and type of endmembers to vary from pixel to pixel. The entire methodology is summarized in steps as follows:

Table 1
Comparative analysis of the existing endmember variability spectral mixture analysis techniques with VECLS.

Sl. no.	Basic principle	Techniques	Genesis	Advantage	Disadvantage	Observation
1	Iterative mixture analysis cycle	MESMA (Multiple Endmember Spectral Mixture Analysis, Roberts et al., 1998)	MESMA allows multiple endmember for each component	• Endmembers are allowed to vary on a pixel basis • Each plausible endmember is accounted by assigning a best-fit (lowest RMSE) to each pixel iteratively	High computation complexity because of iterative nature of the method	Iterative mixture analysis lead to more than one possible combination of pure spectra and sometimes results in the same mixed spectrum which is a ill posedness problem
		Auto MCU (Monte Carlo Spectral Unmixing Model, Asner and Lobell, 2000)	A large number of endmember combinations for each pixel are calculated by randomly selecting spectra from a spectral database to unmix a pixel (also called fuzzy unmixing)	The number of model samples for each of the possible mixture combination is used to compute the probability and confidence of each mixture	It propagates uncertainity in endmember spectra to the final subpixel cover fraction results	
		Endmember Bundles (Bateson et al., 2000)	• From the eigenvectors (obtained through Principal Component Analysis) of the image, bundles of vectors are identified to represent the endmembers. • A linear programming routine determines minimum, mean and maximum fraction of each endmember			
		BSMA (Bayesian Spectral Mixture Analysis, Song, 2005)	BSMA is based on Bayes theorem, it unmixes each pixel with randomly selected combination of endmembers which are represented by a p.d.f.	• Accounts for the probability of spectral signatures, instead of assuming equal probabilities for all endmembers. • Captures spectral variability with least number of endmembers	SMA gives subpixel fractions with almost the same and sometimes even better accuracy than from BSMA except without uncertainty information for the estimates	
2	Spectral feature selection (SFS)	• AutoSWIR (Asner and Lobell, 2000) • Residual Analysis based SFS (Ball et al., 2007) • PCA based SFS (Miao et al., 2006) • DCT based SFS (Li, 2004) • SZU based SFS (Somers et al., 2010b)	• Based on data reduction by selection of wavelengths. • It is robust against spectral variability, i.e., it minimises intra and maximises inter-class variability	• Computation complexity is reduced because of data dimensionality reduction. • Incorporates uncorrelated spectral information. • AutoMCU includes both VIS and NIR bands for feature selection, thereby covering wider wavelength region	AutoSWIR is completely dependent on the availability of high-fidelity SWIR2 region; originally designed for semi-arid region which may not be always true	SZU was found to be better than AutoSWIR and MESMA

Table 1 (*continued*)

Sl. no.	Basic principle	Techniques	Genesis	Advantage	Disadvantage	Observation
3	Spectral weighting	Spectral weighting based technique by Somers et al. (2009b)	• It prioritises spectral bands less sensitive to endmember variability by giving them higher weight in spectral mixture analysis. • The estimated cover fractions are influenced or determined by high reflected energy level in the reflectance bands of the pixel.	The highest reflectance bands for each object can be easily used to estimate class proportions with higher accuracy.	Assigning weightage to endmembers based on dominating wavebands may sometimes be nontrivial.	For vegetation studies, NIR band will dominate the model and VIS bands will dominate marginally.
4	Spectral transformations (ST)	• Tied Spectrum based ST (Asner and Lobell, 2000). • Normalised Spectral Mixture Analysis (NSMA, Wu, 2004). • Derivative Spectral unmixing (DSU, Zhang et al., 2004). • First derivative based ST (Debba et al., 2006). • Wavelet based ST (Li, 2004)	Instead of original reflectance data, transformed / modified spectral information is used for spectral unmixing.	• Landscape features gets highlighted because of spectral band transformation. • Endmember separability increases.	Careful calibration / validation may be required (for example for DSU), as derivatives increase SNR.	Two different transformation methods on the same data may not produce consistent class proportion results such as derivative and wavelet because the number of spectral bands for analysis is only a subset of the original full spectral range.
5	Spectral modelling	• Weighted Linear Spectral Mixture Analysis (Example: Soil Modeling Mixture Analysis – SMMA by Somers et al., 2009a). • MODTRAN radiative transfer model (Eckmann et al., 2008)	Radiative transfer models are used to generate endmember libraries for spectral mixture analysis.	They provide dynamic and robust way to account the spatial and temporal variability.	Each model is specific to an application and cannot be generalised.	SMMA cannot work for a landscape which has no soil.
6	Variable Endmember Constrained Least Square (VECLS)	• Allows the signals within a class to vary from pixel to pixel about a mean spectrum • Endmembers are selected both automatically (through N-FINDR) and using supervised techniques. • Through many instances of a particular endmember, its variability and the interclass variance are accounted by the covariance around the selected endmember mean.		• Non-iterative so less computation complexity. • Method does not involve feature selection, spectral weighting, and transformations. • It is not designed for any specific endmember mixture model and is separately derived for a Gaussian and a generalised case (no assumption of the form of p.d.f.).	The method is applied for simulated and an urban landscape. Its performance on different landscapes has to be assessed to understand the robustness of the technique.	The method need to be applied on different data sets such as hyperspectral with higher number of classes to assess its utility.

Table 2
Mean endmembers and spread around the mean for small, medium and large variability.

Class	Mean endmember in Band 1	Mean endmember in Band 2	Mean endmember in Band 3	Mean endmember in Band 4	Spread to control variability
1	142	136	135	74	0.001
2	81	69	56	203	7
3	140	132	96	7	20

Step-1: Geo-correction of RS data.
Step-2: Decide the number of LC classes.
Step-3: Derive individual endmembers from the image.
Step-4: Correlate endmembers to ground conditions (LC classes).
Step-5: Select many instances of endmembers to account for the statistical variability.
Step-6: Represent each class by its mean and variance-covariance matrix.
Step-7: Apply VECLS algorithm.
Step-8: Obtain abundance map for each class.
Step-9: Validate abundance maps with ground truths using correlation, RMSE, and BDF plots.

4.1. Simulated data

Spectral libraries of three minerals – alunite (endmember1), buddingtonite (endmember2), and kaolinite (endmember3) available at http://speclib.jpl.nasa.gov/ were used to generate simulated data, which comprises of three classes. Also, to accommodate for the dimensionality constraint in unmixing (Settle and Drake, 1993), four simulated spectral wavebands of 100×100 dimensions were considered. The spectral responses of each class in each waveband were varied (from small to medium to large) in separate experiments to illustrate the impacts of differences in intra-class variation.

Initially, means of different classes (Table 2) were taken to define the class endmember spectra and then used to generate abundance maps for validating the output of VECLS algorithm. Here, each pixel was obtained from a LMM and the endmembers of each category was drawn from a Gaussian distribution where the mean of each endmember can be set and the variability can be controlled.

Artificial bands are assumed to be of the form: mean + Gaussian perturbation given by covariance, i.e.,

- endmember 1 = mean 1 + random perturbation;
- endmember 2 = mean 2 + random perturbation;
- endmember 3 = mean 3 + random perturbation;

where random perturbation is a Gaussian random variable of 0 mean and specific variance. So,

$$\begin{aligned}\text{artificial band} = {} & \text{abundance1} \times \text{endmember1} \\ & + \text{abundance2} \times \text{endmember2} \\ & + \text{abundance3} \times \text{endmember3}. \end{aligned} \quad (27)$$

The statistical properties of each simulated band are given in Table 3. A multitude of LMMs were applied with different endmembers and a series of sub-pixel class composition estimates were obtained for a pixel of given spectral response. The bands were spatially degraded to 50×50 dimension (half the spatial resolution of the original image) and to 10×10 dimension (one tenth of the original image dimension) to study the impact of endmember variability at different spatial scales. In this way, we could analyse not only the impact of variable endmembers, but also the impact of variability in endmembers with respect to change in spatial resolutions. In another set of experiments, covariance of all the endmembers were made zero, i.e., assuming each endmember is being represented by only one spectrally pure pixel and there is no variation within an endmember. The idea behind doing this was to compare the performance of the algorithm in two complementary cases, namely, when the endmembers have (i) variability, (ii) no variability.

It was ensured that there are instances of 100% class proportions in the three abundance maps generated using simulated data. These pixels were then mapped to the original bands and corresponding pixel values were extracted as endmembers. User defined means and spread around the mean could be incorporated into the simulated data and hence, the endmembers in the 4 bands were cross verified with the class means. Endmembers were also visualised using scatterplots (Fig. 2) which shows location of classes defined by the means in simulated data with small, medium and large variability, where each class occupies an area of the feature space. It is obvious that any one point in the feature space can be associated with a variety of class compositions.

4.2. Remote sensing data

The VECLS algorithm was assessed for its performance in unmixing mixed pixels of various spatial and spectral resolutions. Initially, IKONOS 4 bands MS data of 4 m spatial resolution were fused with IKONOS 1 m Panchromatic (PAN) band using Smoothing Filter based Intensity Modulation (SFIM) fusion (Liu, 2000) based on comparative analysis of the image fusion results (Kumar et al., 2009, 2011a). Training pixels were taken from the False Colour Composite (FCC) and supervised classification using Maximum Likelihood Classifier (MLC) (Duda et al., 2000; Richards and Jia, 2006; Zheng et al., 2005) was performed on the fused data (1 m) to classify the image into 2 classes

Table 3
Statistical properties of the simulated data.

Bands	Minimum	Maximum	Range	Mean	Variance	Variation coefficient (%)
Small variability						
1	80.99	142.00	61.02	124.72	353.95	15.09
2	69.03	136.03	67.01	116.51	419.93	17.59
3	55.96	134.95	78.99	102.34	548.70	22.89
4	7.02	202.99	195.97	90.46	2652.17	56.93
Medium variability						
1	76.42	149.98	73.56	124.71	358.24	15.18
2	65.08	141.18	76.09	116.50	424.60	17.69
3	50.49	139.45	89.26	102.33	553.69	22.99
4	5.12	205.75	200.63	90.47	2657.12	56.98
Large variability						
1	69.36	153.70	84.34	124.78	366.32	15.34
2	59.84	149.93	90.09	116.60	435.10	17.89
3	44.94	147.47	102.54	102.43	560.94	23.12
4	2.87	207.81	204.94	90.33	2661.18	57.11

(vegetation, non-vegetation), 3 classes (urban, vegetation and water) and 4 classes (urban, vegetation, water and open area). The overall accuracy of the classified images were 98% (2 classes), 96% (3 classes) and 93% (4 classes) respectively. These classified maps were used as references to validate the sub-pixel maps obtained using VECLS and CLS. A series of experiments with varying resolutions and varying classes (2, 3 and 4) were carried out to illustrate the performance of the proposed algorithm. The details of the data (IKONOS PAN (1 m) and MS (4 m), Landsat ETM+ MS (25 m) and MODIS 7 bands (250 m)) used are provided in Table 4.

The study area (Fig. 3) is a part of Bangalore City, India which is highly urbanised with considerable spectral variation (for example due to buildings with concrete roofs, tiled roofs, asbestos, asphalt, etc.) that exhibit high degrees of spectral heterogeneity on fine scales. The scene has dense buildings, bus stand, railway station, tarred roads with flyovers, parks, race course and lakes. There are few open areas (such as playground, walk ways and vacant land). This scene was appropriate to judge the performance of VECLS with highly contrasting and heterogeneous features at different spatial resolutions. We had little prior knowledge of the appropriate spatial scale for interpreting the fractions generated for an urban area. Hence, varying the spatial scale allowed us to investigate the impact of scales based on size of sampling unit, as well as to consider how confident are the estimates of LC fractions that might vary with spatial scale.

Endmembers were extracted from IKONOS MS, Landsat and MODIS data using N-FINDR algorithm (Boardman, 1995). The advantage of image endmembers is that they can be collected at the same scale as the image, therefore, endmembers are easier to associate with image features (Rashed et al., 2003) but have some associated error, which varies with the scale of the measurement used and the scale of intrinsic spatial variation (Settle, 2006). The N-FINDR algorithm is briefly given below.

1. Let N denote the number of classes or endmembers to be identified.
2. Perform a principal component analysis (PCA)-decomposition of the data and reduce the dimension of the data to $N-1$. In what follows, we assume that the data are transformed to $N-1$ dimension PCA space.
3. Pick N pixels from the set and compute the simplex volume generated by the spectra of the N pixels. The volume of the simplex is proportional to

$$V = \det \begin{vmatrix} 1 & 1 & \cdots & 1 \\ e_{11} & e_{12} & \cdots & e_{1M} \\ e_{21} & e_{22} & \cdots & e_{2M} \\ \cdots & \cdots & \cdots & \cdots \\ e_{M-11} & e_{M-12} & \cdots & e_{M-1M} \end{vmatrix} \tag{28}$$

4. Replace each endmember with the spectrum of each pixel in the dataset and recompute the simplex volume. If the volume increases, the spectrum of the new pixel is retained as a potential endmember.

As the endmembers are at the extreme points of the convex hull, the N-FINDR algorithm tries to find out those pixels whose convex hull generated by their spectrum contains the spectra of all the other pixels achieved by maximising the volume of the simplex (convex hull). These steps are executed iteratively considering all the pixels and the final set of spectra retained are taken to be the endmembers (Winter, 1999).

These endmembers were also identified in the three FCCs and individual spectral bands of all the sensor data. Many instances of similar endmembers per class were chosen from the FCC and the scatterplots, and were incorporated into the VECLS algorithm. VECLS was applied on

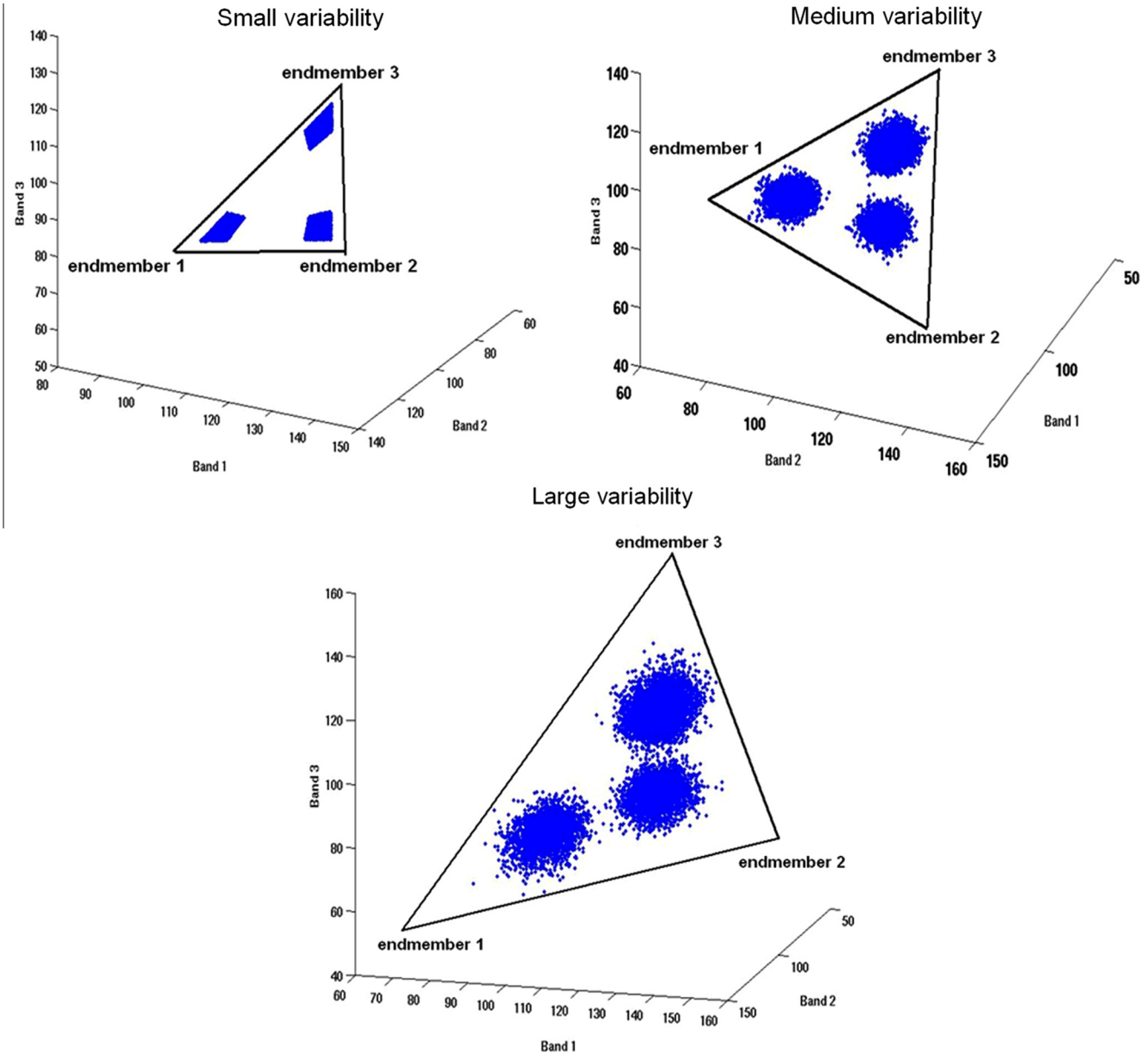

Fig. 2. Endmember locations defined by the extreme pixels in small, medium and large variability data sets for three classes.

Table 4
Remote sensing datasets used for validating VECLS algorithm.

Data	Spectral bands	Spatial resolution	Dimension	Two classes	Three classes	Four classes
IKONOS PAN and MS fused	4	1 m	8000 × 8000	Vegetation, non-vegetation	Urban, vegetation, water	Urban, vegetation, water, open area
IKONOS	4	4 m	2000 × 2000	Vegetation, non-vegetation	Urban, vegetation, water	–
Landsat	6	30 m resampled to 25 m	320 × 320	Vegetation, non-vegetation	Urban, vegetation, water	Urban, vegetation, water, open area
MODIS	7	250 m	32 × 32	Vegetation, non-vegetation	Urban, vegetation, water	Urban, vegetation, water, open area

each dataset to obtain the abundance maps for 2, 3 and 4 classes. Since IKONOS has only 4 spectral bands, only 3 target classes could be used due to dimensionality constraints. The covariance of all the endmembers were also assumed zero to assess the performance of the algorithm in the absence of variability. This would give

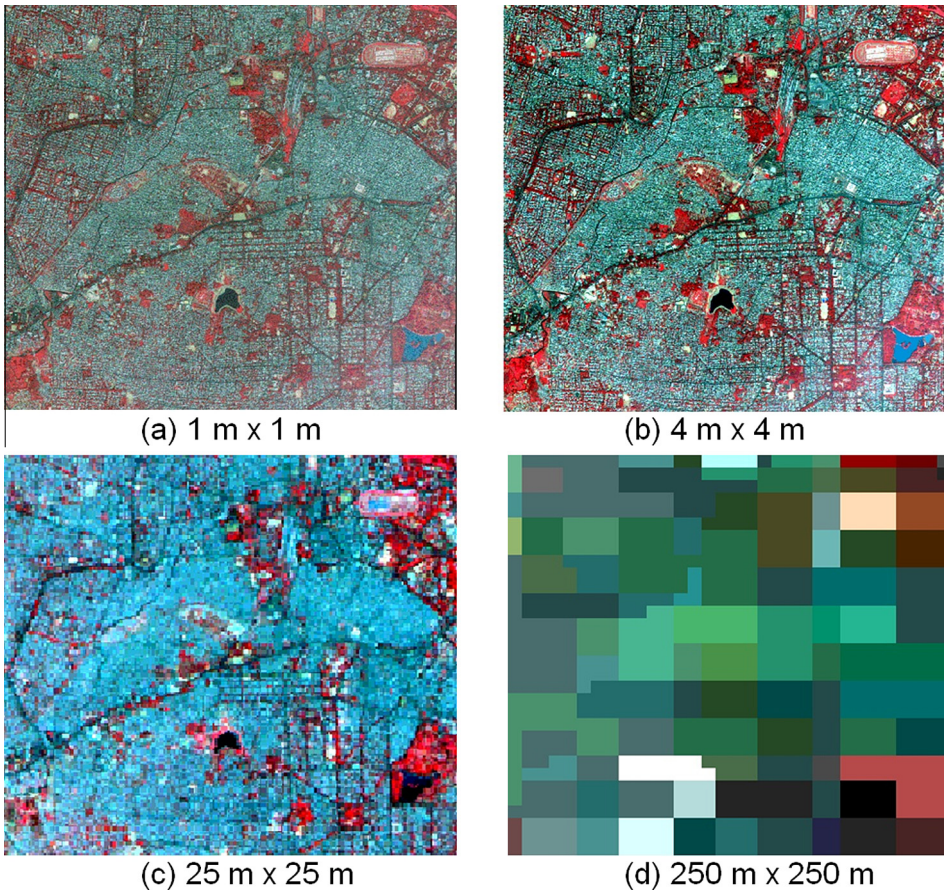

Fig. 3. False Colour Composite of the study area from (a) IKONOS (PAN and Multispectral fused), (b) IKONOS Multispectral, (c) Landsat ETM+ and (d) MODIS.

the relative benefits of the proposed method and highlight the advantages of considering variability in endmembers.

5. Results

5.1. Simulated data

Accuracy assessment of the abundance maps for 3 classes with small, medium and large variability obtained from VECLS algorithm with reference abundance maps is depicted in Tables 5–7 respectively. Figs. 4–6 shows the impact of intra-class variability on the accuracy of unmixing. Note that there are no pixels with abundances from 20% up to 70% in the abundance maps. The scatter in the relationship between predicted and actual class composition increases with an increase in the degree of intra-class spectral variation (from Figs. 4–6 for each class), reducing the accuracy of the sub-pixel class composition estimates derived in Table 5. However, these accuracies are far better when compared to abundance estimation without endmember variability, also evident from Table 5.

The correlation and RMSE between predicted and actual/real/reference proportions with spatially degraded (down sampled) images are shown in Table 6 (at 50% of the original image size, i.e. 50×50) and Table 7 (at 10% of the original image size, i.e., 10×10). It is evident from these Tables that VECLS has an improved accuracy over CLS method. That is, the variability in endmembers has been accounted by the proposed algorithm than assuming single endmember per class. By degrading the images, it was observed that the accuracy comes down marginally and there is no drastic reduction. However, one important conclusion that can be drawn is that it is difficult to capture more variability with higher accuracy. Controlled variability and the effect of changing resolution resulted in two important findings: (i) As variability increases, the accuracy of classification decreases. In fact, the accuracy of sub-pixel fraction estimates linearly decreases with intra-class variability (Barducci and Mecocci, 2005; Settle, 2006). This is rational because higher the intra-class variability, more is the likelihood that the actual spectral characteristics of the endmembers in a pixel will deviate from the fixed endmembers. (ii) Down sampling of image pixels (from high to low resolution) affects the overall accuracy marginally with linear unmixing when (a) the endmembers have been identified properly at each original image resolution with respect to the ground conditions and, (b) the data fit well into the linear model.

Table 5
Accuracy of prediction derived from low, medium and large variability data compared to absence of endmember variability (single spectra for each endmember) for 100 × 100 dimension images.

Class	VECLS	CLS (0 covariance)	VECLS	CLS (0 covariance)
	Correlation coefficient (r) ($p < 2.2e^{-16}$)		RMSE	
Small variability				
1	0.9998	0.7332	0.0029	0.2312
2	0.9999	0.7403	0.0005	0.2077
3	0.9999	0.7406	0.0004	0.2088
Medium variability				
1	0.9948	0.7155	0.0386	0.2506
2	0.9989	0.7380	0.0153	0.2104
3	0.9954	0.7321	0.0308	0.2181
Large variability				
1	0.9851	0.7897	0.0563	0.2114
2	0.9968	0.7344	0.0259	0.2712
3	0.9850	0.8076	0.0561	0.1399

Table 6
Accuracy of prediction derived from low, medium and large variability data compared to absence of endmember variability at half the original image dimension.

Class	VECLS	CLS (0 covariance)	VECLS	CLS (0 covariance)
	Correlation coefficient (r) ($p < 2.2e^{-16}$)		RMSE	
Small variability				
1	0.9944	0.7105	0.0039	0.1732
2	0.9988	0.7211	0.0015	0.1223
3	0.9988	0.7213	0.0015	0.1221
Medium variability				
1	0.9921	0.7341	0.0089	0.1022
2	0.9973	0.7241	0.0011	0.1210
3	0.9921	0.7222	0.0088	0.1289
Large variability				
1	0.9821	0.7879	0.0673	0.0779
2	0.9933	0.7339	0.0079	0.1052
3	0.9841	0.8069	0.0601	0.0649

Table 7
Accuracy of prediction derived from low, medium and large variability data compared to absence of endmember variability at one-tenth of the original image dimension.

Class	VECLS	CLS (0 covariance)	VECLS	CLS (0 covariance)
	Correlation coefficient (r) ($p < 2.2e^{-16}$)		RMSE	
Small variability				
1	0.9911	0.7101	0.0029	0.2111
2	0.9985	0.7199	0.0009	0.2101
3	0.9983	0.7201	0.0011	0.2091
Medium variability				
1	0.9889	0.7977	0.0005	0.2061
2	0.9890	0.7810	0.0004	0.2405
3	0.9900	0.7001	0.0414	0.2813
Large variability				
1	0.9237	0.7297	0.1841	0.2417
2	0.9122	0.7544	0.1977	0.2106
3	0.9114	0.8076	0.1985	0.1917

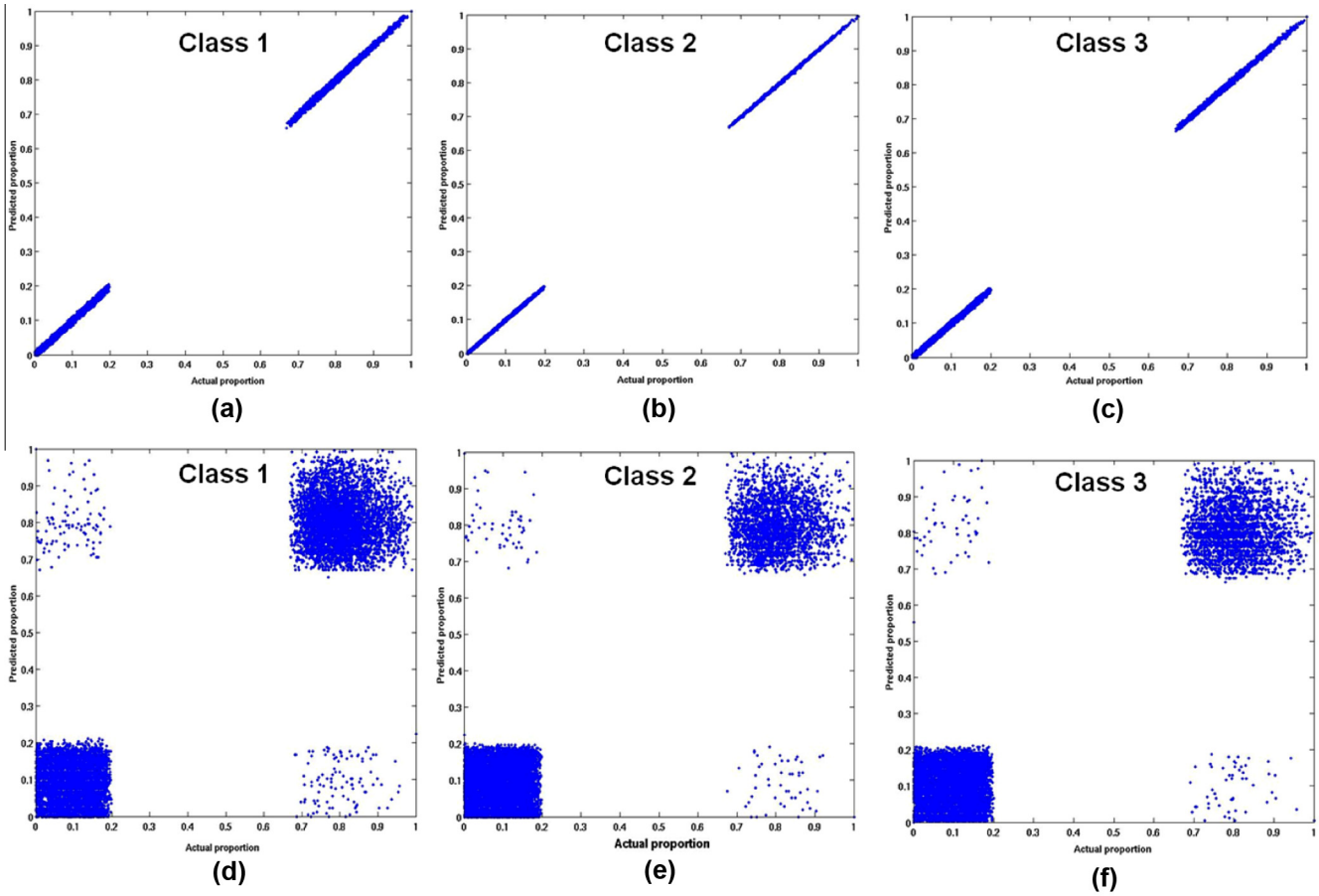

Fig. 4. The impact of small intra-class variability on the accuracy of unmixing using VECLS (a–c) and using CLS without variability (d–f).

5.2. Remote sensing data

The IKONOS, Landsat ETM+ and MODIS images were unmixed using VECLS method taking into account covariance due to variability in endmembers and later, subsequently assuming endmembers with zero covariance for comparison (Fig. 7). The MODIS unmixed images are not shown in Fig. 7 due to space constraint. The obtained abundances were validated using correlation and RMSE as shown in Tables 8–10.

Figs. 8–10 indicates that, in general, abundances obtained from VECLS technique are much better than CLS method. For 2 and 3 classes, with decrease in the spatial resolution, the accuracy also decreases. However, this may not be always true when using Landsat and MODIS data in case of vegetation (Fig. 8) and in case of vegetation, water and open area for 4 classes (Fig. 10). The accuracy depends on the actual number of endmembers present in the image correlated to ground conditions and also the capability of the spectral bands to distinguish those objects.

Also, with a very high spatial resolution data such as IKONOS with 4 m spatial resolution, LMM would not be always very useful. Ideally, in this case, we may get abundances as 1 or 0 since there are high chances that the intrinsic scale of objects on the ground may be of the order of 1 IKONOS MS pixel. On the other hand, LMM might work best for low spatial resolution and high spectral resolution (such as MODIS) as evident from Fig. 10 for vegetation, water and open area classes. Since class separability depends on the number of spectral bands, so the separation between endmembers of different classes is important for obtaining higher accuracy. As also evident from simulated data analysis, increase in variability may reduce classification accuracy, but degrading the spatial resolution may not always decrease the accuracies of individual classes compared to accuracies obtained from classification of high spatial resolution data, provided a minimum residual error linear model with proper endmember selection is achieved. Urban class was identified with higher accuracy in IKONOS and Landsat bands compared to MODIS bands. Usually, urban areas have more heterogeneity with contrasting features and variability compared to other LC classes. Moreover, spatial extent of the urban objects are typically of high to medium spatial resolution pixel size, so Landsat data would be appropriate for urban land use/land cover types of studies while IKONOS data would be best for micro level urban studies.

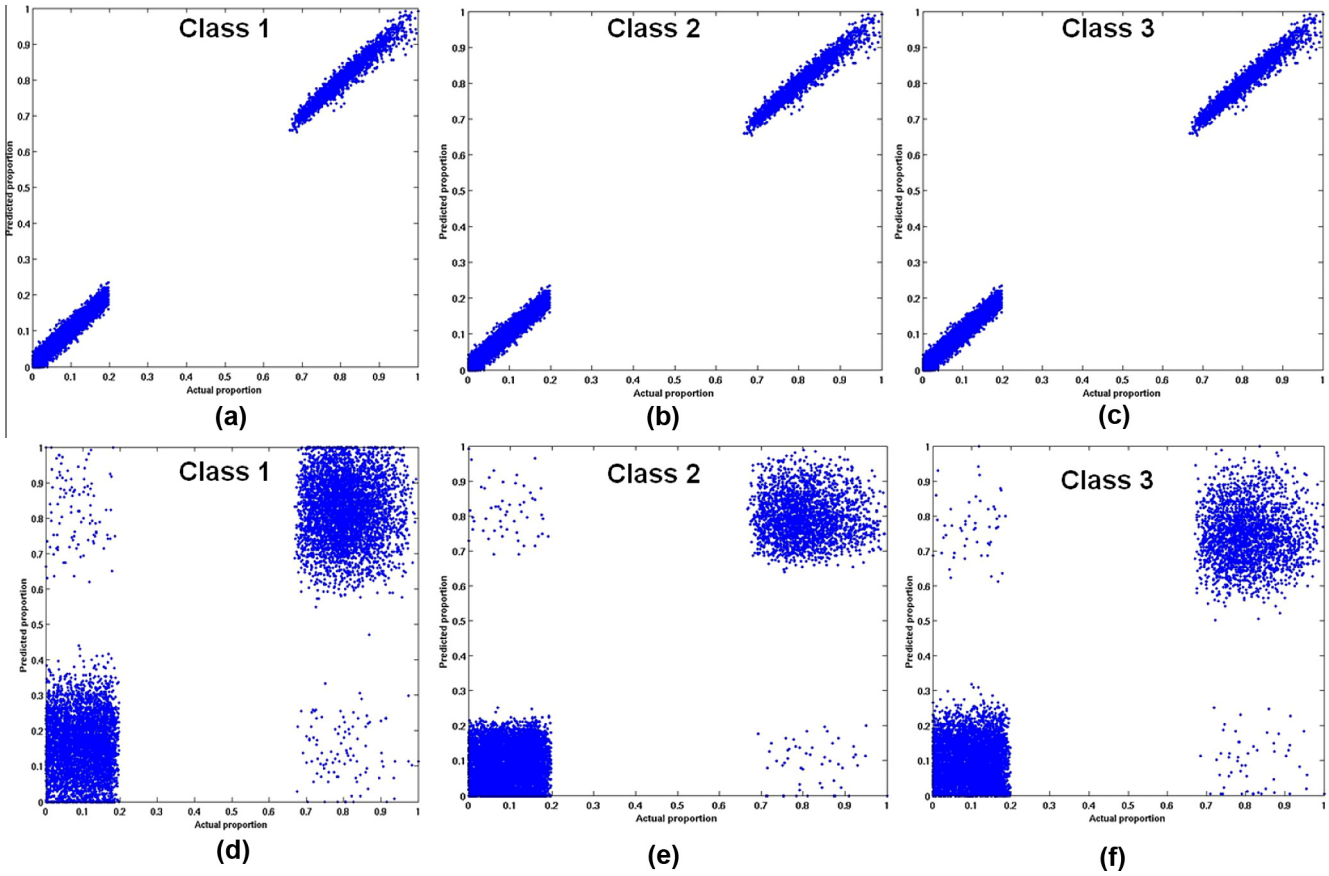

Fig. 5. The impact of medium intra-class variability on the accuracy of unmixing using VECLS (a–c) and using CLS without variability (d–f).

6. Discussion

Soft classification methods have attracted considerable attention for reducing the mixed pixel problem that is often encountered in RS applications. The exact nature of the derived unmixing results is a function of classification algorithm and endmember definitions. Correlation for all the estimated classes with actual/reference proportion of those classes greatly improved when endmembers were selected based on the spectral variability of materials within the scene. The effect of decreasing correlation between reference and modelled fractions due to decrease in spatial resolution was an expected result for several reasons: (a) decreasing the pixel size would increase the impact of geolocation error and this would affect accuracy assessment while comparing the results with a high spatial resolution classified reference map; (b) the signal recorded at the sensor for a single pixel is affected by the spectral properties of surrounding pixels (Forster, 1985; Townshend et al., 2000); and (c) the process of averaging fractions over larger areas reduces the variance of each dataset thereby, decreases correlation between fractions, with the assumption that the means of the two datasets are similar. Actually, similarity between endmembers results in a high correlation between the endmember spectra, which in turn leads to an unstable inverse matrix and a dramatic drop in estimation accuracy (Gong and Zhang, 1999). Under ideal conditions, most accurate fractional estimates can be achieved using the minimum number of endmembers required to account spectral variability within a mixed pixel (Sabol et al., 1992). Fractional errors occur either when too few endmembers are used resulting in spectral information that cannot be accounted by the existing endmembers, or too many, in which case minor departures between measured and modelled spectra are often assigned to an endmember that is used in the model, but not actually present (Roberts et al., 1998). Urban environments are particularly difficult for a simple mixture model because a single endmember cannot account for considerable spectral variation within a class. In contrast, endmember variability can account for within-class variability and thus is likely to be more suitable for urban RS (Franke et al., 2009). Using the VECLS approach, pixel-scale limits in spectral dimensionality were acknowledged while also accounting for considerable spectral variability within a scene. The uncertainties in endmember fraction estimates that are usually caused by brightness differences due to the wide FOV (Field of view) of sensors or particularly due to the complex structure of urban objects are minimised (Franke et al., 2009). This work highlights that it is not sufficient to use a spectral

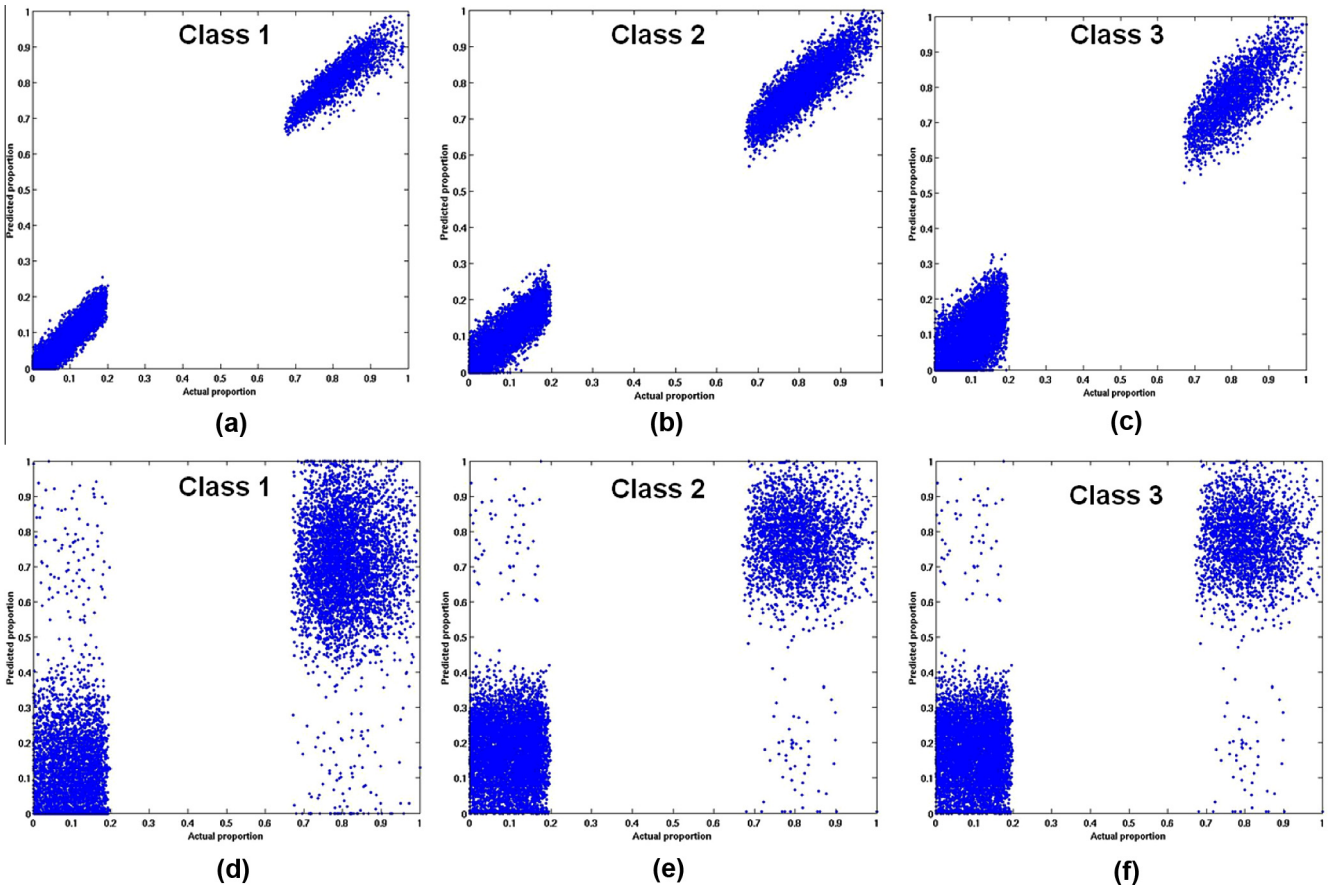

Fig. 6. The impact of large intra-class variability on the accuracy of unmixing using VECLS (a–c) and using CLS without variability (d–f).

library based on the most representative endmembers of each category. The 'purest' endmember fractions are not necessarily representative of materials within the scene and representative spectra may not necessarily be selected as 'pure' endmembers (Song, 2005). An endmember that is most representative of its class, in this case of endmember selection may not capture LC with distinct spectra that occupy small areas within the scene (Powell et al., 2007). Therefore, accounting endmember variability for each class is important for estimating correct class proportions.

Usually, two common problems are encountered while identifying endmembers and performing unmixing. Firstly, the sub-pixel abundances generated generally do not correspond to a single class of LC materials. For example, in densely builtup areas, bare soil tend to occur and mix with roof tiles made up of clay in addition to some surrounding materials. This results in wrong estimation of LC fractions. Secondly, when two classes of materials exist as mixtures within a sub-pixel, such as soil mixed with vegetation, the chances of identifying proper endmember and correct estimation of fractions reduces. In the absence of pure pixels, alternative algorithms (Plaza et al., 2002 and Plaza et al., 2004) can be used for endmember extraction. VECLS can be applied in other cities and different landscapes with diverse natural environments to assess its generality. There are several challenges on which future research can be based:

(i) Incorporating endmember variability in the absence of endmembers.
(ii) Integration of spatial, temporal and spectral information for reducing endmember variability.
(iii) Combining non-linear mixture models (Kumar et al., 2012) with VECLS method to account both the effects of endmember variability and multiple scattering.
(iv) Development of methods to account for the bidirectional reflectance (Asner et al., 1997), adjacency effects and atmospheric interferences (Settle, 2005; Somers et al., 2011).

7. Conclusion

In general, most cases of sub-pixel analysis assume that classes may be described by unique endmembers. However, due to class spectral variability, no single spectrum can describe a class adequately. As a result, distribution of possible class compositions for each pixel exists, where accuracy of sub-pixel class abundances are functions of

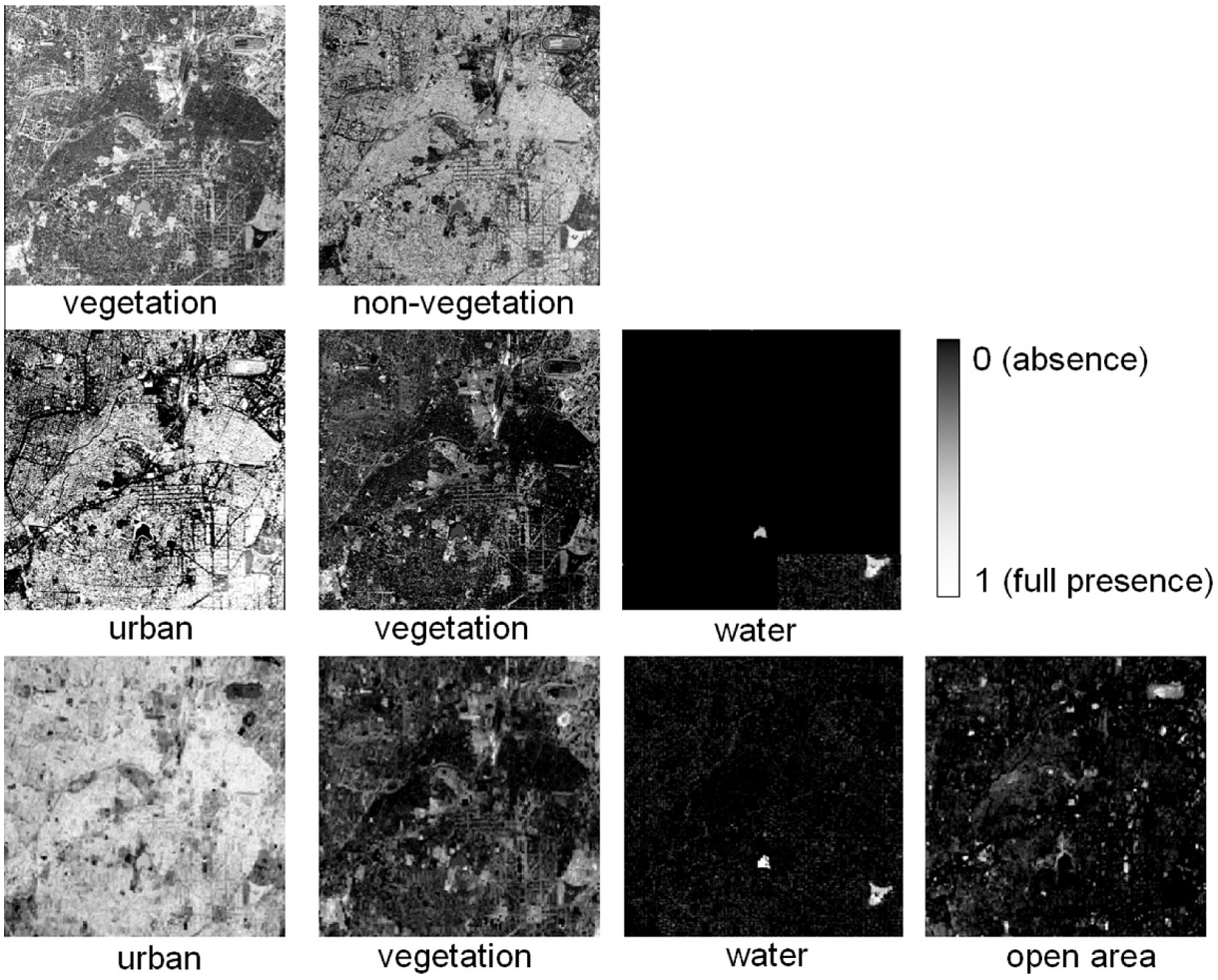

Fig. 7. Classified output for two classes (vegetation, non-vegetation), three classes (urban, vegetation and water) from IKONOS, and four classes (urban, vegetation, water and open area) from Landsat ETM+.

Table 8
Accuracy of prediction for IKONOS images for 2 and 3 classes with and without endmember variability.

IKONOS (4 m)				
	VECLS	CLS (0 covariance)	VECLS	CLS (0 covariance)
2 Class	Correlation coefficient (r) ($p < 2.2e^{-16}$)		RMSE	
Vegetation	0.9951	0.8122	0.0527	0.1745
Non-vegetation	0.9751	0.8222	0.0751	0.1688
3 Class	Correlation coefficient (r) ($p < 2.2e^{-16}$)		RMSE	
Urban	0.9307	0.7998	0.0715	0.2173
Vegetation	0.9461	0.7843	0.0602	0.2207
Water	0.9747	0.7678	0.0321	0.0302

intra-class spectral variations. In this communication, we proposed a new method – variable endmember constrained least square (VECLS) which has the ability to incorporate the intra-class variability of the spectral signatures in the unmixing process. The covariance matrix for each endmember obtained from the original bands was accounted in classification for the variability in each class. The results of the algorithm implementation on computer simulated data with small, medium and large variability resulted in an average correlation increment of 0.25. The application on RS data such as IKONOS, Landsat ETM+ and MODIS also showed promising results with increased average correlation for different number of classes compared to absence of endmember variability, demonstrating the effectiveness of this approach.

Table 9
Accuracy of prediction for Landsat images for 2, 3 and 4 classes with and without endmember variability.

Landsat (25 m)				
	VECLS	CLS (0 covariance)	VECLS	CLS (0 covariance)
2 Class	Correlation coefficient (r) ($p < 2.2e^{-16}$)		RMSE	
Vegetation	0.9307	0.7998	0.0744	0.2109
Non-vegetation	0.9461	0.7843	0.0609	0.2346
3 Class	Correlation coefficient (r) ($p < 2.2e^{-16}$)		RMSE	
Urban	0.8905	0.7290	0.1165	0.2846
Vegetation	0.9104	0.7967	0.0935	0.2195
Water	0.9214	0.7519	0.0827	0.2516
4 Class	Correlation coefficient (r) ($p < 2.2e^{-16}$)		RMSE	
Urban	0.8413	0.6714	0.1424	0.3375
Vegetation	0.8525	0.6385	0.1589	0.3787
Water	0.8825	0.6192	0.1205	0.3926
Open area	0.8161	0.6439	0.1749	0.3596

Table 10
Accuracy of prediction for MODIS images for 2, 3 and 4 classes with and without endmember variability.

MODIS (250 m)				
	VECLS	CLS (0 covariance)	VECLS	CLS (0 covariance)
2 Class	Correlation coefficient (r) ($p < 2.2e^{-16}$)		RMSE	
Vegetation	0.9273	0.7761	0.0911	0.2389
Non-vegetation	0.9137	0.7561	0.0855	0.2522
3 Class	Correlation coefficient (r) ($p < 2.2e^{-16}$)		RMSE	
Urban	0.8621	0.7036	0.1490	0.3054
Vegetation	0.8882	0.7055	0.1229	0.3003
Water	0.8414	0.7165	0.1620	0.2946
4 Class	Correlation coefficient (r) ($p < 2.2e^{-16}$)		RMSE	
Urban	0.8231	0.6606	0.1777	0.4470
Vegetation	0.8731	0.6804	0.12093	0.3206
Water	0.8930	0.6842	0.1142	0.3292
Open area	0.7971	0.6492	0.2105	0.3629

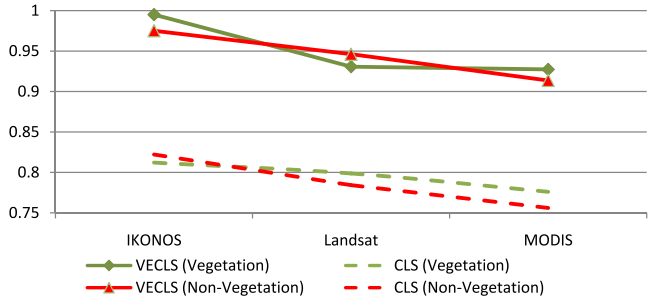

Fig. 8. Correlation between actual and predicted proportion for two classes with changing spatial resolutions.

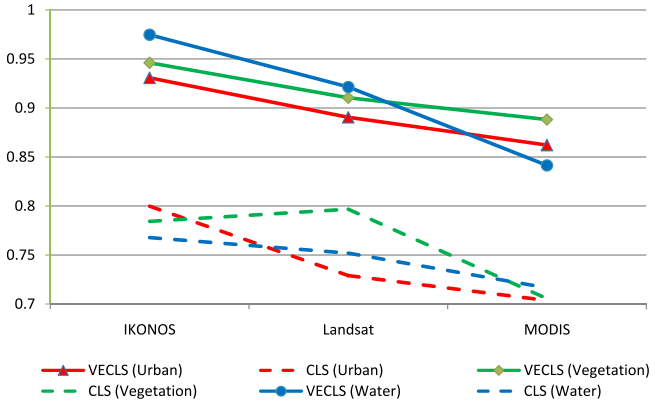

Fig. 9. Correlation between actual and predicted proportion for three classes with different sensor data.

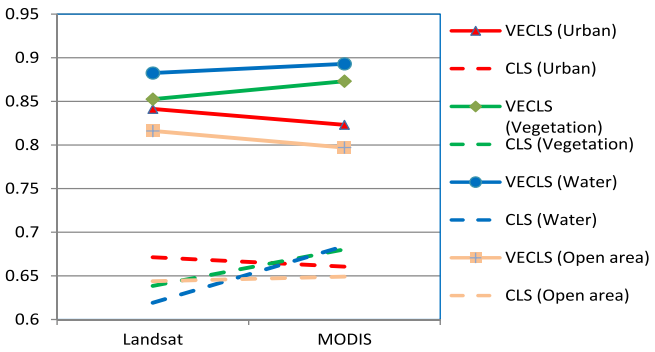

Fig. 10. Correlation between actual and predicted proportion for four classes with different sensor data.

Acknowledgement

We are grateful to Indian Institute of Science for financial and infrastructure support. Global Land Cover Facility (GLCF) is appreciated for providing the Landsat and MODIS data. We thank GeoEye Foundation, USA for providing IKONOS imagery for Greater Bangalore City.

References

Asner, G.P., 1998. Biophysical and biochemical sources of variability in canopy reflectance. Remote Sens. Env. 64, 234–253.

Asner, G.P., Lobell, D.B., 2000. A biogeophysical approach for automated SWIR unmixing of soils and vegetation. Remote Sens. Env. 74, 99–112.

Asner, G.P., Wessman, C.A., Privette, J.L., 1997. Unmixing the directional reflectances of AVHRR subpixel landcovers. IEEE Trans. Geosci. Remote Sens. 35, 868–878.

Ball, J.E., Bruce, L.M., Younan, N.H., 2007. Hyperspectral pixel unmixing via spectral band selection and DC-insensitive singular value decomposition. IEEE Geosci. Remote Sens. Let. 4, 382–386.

Barducci, A., Mecocci, A., 2005. Theoretical and experimental assessment of noise effects on least-squares spectral unmixing of hyperspectral images. Optical Engineering, 44, Art. no. 087008.

Bateson, C.A., Asner, G.P., Wessman, C.A., 2000. Endmember bundles: A new approach to incorporating endmember variability into spectral mixture analysis. IEEE Trans. Geosci. Remote Sens. 38, 1083–1094.

Boardman, J., 1995. Analysis, understanding and visualization of hyperspectral data as a convex set in n-space. International SPIE symposium on Imaging Spectrometry, Orlando, Florida, 23–36.

Carlson, T.N., Sanchez-Azofeifa, G.A., 1999. Satellite remote sensing of land use changes in and around San José. Costa Rica. Remote Sens. Env. 70, 247–256.

Debba, P., Carranza, E.J.M., vanderMeer, F.D., Stein, A., 2006. Abundance estimation of spectrally similar minerals by using derivative spectra in simulated annealing. IEEE Trans. Geosci. Remote Sens. 44, 3649–3658.

Dennison, P.E., Roberts, D.A., 2003. Endmember selection for multiple endmember spectral mixture analysis using endmember average RMSE. Remote Sens. Env. 87, 123–135.

Dobigeon, N., Moussaoui, S., Coulon, M., Tourneret, J.Y., Hero, A.O., 2009. Joint Bayesian endmember extraction and linear unmixing for hyperspectral imagery. IEEE Trans. Signal Process. 57, 4355–4368.

Duda, R.O., Hart, P.E., Stork, D., 2000. Pattern Classification, second ed. Wiley-Interscience Publication, New York, ISBN 9814-12-602-0.

Eckmann, T.C., Roberts, D.A., Still, C.J., 2008. Using multiple endmember spectral mixture analysis to retrieve subpixelfire properties from MODIS. Remote Sens. Env. 112, 3773–3783.

Foody, G.M., Doan, H.T.X., 2007. Variability in soft classificaton prediction and its implications for sub-pixel scale change detection and super resolution mapping. Photogramm. Engg. Remote Sens. 73 (8), 923–933.

Forster, B.C., 1985. An examination of some problems and solutions in monitoring urban areas from satellite platforms. Int. J. Remote Sens. 6, 139–151.

Franke, J., Roberts, D.A., Halligan, K., Menz, G., 2009. Hierarchical Multiple Endmember Spectral Mixture Analysis (MESMA) of hyperspectral imagery for urban environments. Remote Sens. Env. 113, 1712–1723.

Gong, P., Zhang, A., 1999. Noise effect on linear spectral unmixing. J. GIS 5, 52–57.

Kumar, U., Kerle, N., Ramachandra, T.V., 2008. Constrained linear spectral unmixing technique for regional land cover mapping using MODIS data. In: Khaled Elleithy (Ed.), Innovations and Advanced Techniques in Systems, Computing Sciences and Software Engineering. Springer, Berlin, pp. 87–95.

Kumar, U., Mukhopadhyay, C., Ramachandra, T.V., 2009. Pixel based fusion using IKONOS imagery. Int. J. Recent Trends Eng. (Comput. Sci.) 1 (1), 178–182.

Kumar, U., Dasgupta, A., Mukhopadhyay, C., Joshi, N.V., Ramachandra, T.V., 2011a. Comparison of 10 multi-sensor image fusion paradigms for IKONOS images. Int. J. Res. Rev. Comput. Sci. 2(1), 42–47.

Kumar, U., Kerle, N., Punia, M., Ramachandra, T.V., 2011b. Mining land cover information using multilayer perceptron and decision tree from MODIS data. J. Indian Soc. Remote Sens. 38 (4), 592–603.

Kumar, U., Kumar Raja, S., Mukhopadhyay, C., Ramachandra, T.V., 2011c. Hybrid Bayesian Classifier for Improved Classification Accuracy. IEEE Geosci. Remote Sens. Lett. 8(3), 473–476.

Kumar, U., Kumar Raja, S., Mukhopadhyay, C., Ramachandra, T.V., 2012. A Neural network based hybrid mixture model to extract information from non-linear mixed pixels. Information 3 (3), 420–441.

Lambin, E.F., Turner, B.L., Geist, H.J., Agbola, S.B., Angelsen, A., Bruce, J.W., et al., 2001. The causes of land-use and land-cover change: Moving beyond the myths. Global Env. Change 11, 261–269.

Li, J., 2004. Wavelet-based feature extraction for improved endmember abundance estimation in linear unmixing of hyperspectral signals. IEEE Trans. Geosci. Remote Sens. 42, 644–649.

Liu, J.G., 2000. Smoothing filter-based intensity modulation: A spectral preserve image fusion technique for improving spatial details. Int. J. Remote Sens. 21 (18), 3461–3472.

Lu, D., Weng, Q., 2004. Spectral mixture analysis of the urban landscape in Indianapolis with Landsat ETM+ imagery. Photogramm. Eng. Remote Sens. 70, 1053–1062.

Martinez, P.J., Perez, R.M., Plaza, A., Aguilar, P.L., Cantero, M.C., Plaza, J., 2006. Endmember extraction algorithms from hyperspectral images. Ann. Geophys. 49, 93–101.

Miao, L., Qi, H., 2007. Endmember extraction from highly mixed data using minimum volume constrained nonnegative matrix factorization. IEEE Trans. Geosci. Remote Sens. 45, 765–777.

Miao, X., Gong, P., Swope, S., Pu, R., Carruthers, R., Anderson, G.L., et al., 2006. Estimation of yellow starthistle abindance through CASI-2 hyperspectral imagery using linear spectral mixture models. Remote Sens. Env. 101, 329–341.

Myint, S.W., Lam, N.S.N., Tyler, J.M., 2004. Wavelets for urban spatial feature discrimination: comparisons with fractal, spatial autocorrelation, and spatial co-occurrence approaches. Photogramm. Eng. Remote Sens. 70, 803–812.

Nielsen, A.A., 2001. Spectral mixture analysis: Linear and semi-parametric full and iterated partial unmixing in multi-and hyperspectral image data. Int. J. Comput. Vision 42 (1), 17–37.

Petrou, M., Foschi, P.G., 1999. Confidence in linear spectral unmixing of single pixels. IEEE Trans. Geosci. Remote Sens. 37 (1), 624–626.

Plaza, A., Martinez, P., Perez, R., Plaza, J., 2002. Spatial/spectral endmember extraction by multidimensional morphological operations. IEEE Trans. Geosci. Remote Sens. 40 (9), 2025–2041.

Plaza, A., Martinez, P., Perez, R., Plaza, J., 2004. A quantitative and comparative analysis of endmember extraction algorithms from hyperspectral data. IEEE Trans. Geosci. Remote Sens. 42 (3), 650–663.

Plaza, A., Martinez, P., Plaza, J., Perez, R., 2005. Dimensionality reduction and classification of hyperspectral image data using sequences of extended morphological transformations. IEEE Trans. Geosci. Remote Sens. 43, 466–479.

Powell, R.L., Roberts, D.A., Dennison, P.E., Hess, L.L., 2007. Sub-pixel mapping of urban land cover using multiple endmember spectral mixture analysis: Manaus, Brazil. Remote Sens. Env. 106, 253–267.

Rashed, T., Weeks, J.R., Roberts, D.A., Rogan, J., Powell, R.L., 2003. Measuring the physical composition of urban morphology using multiple endmember spectral mixturemodels. Photogramm. Eng. Remote Sens. 69 (9), 1011–1020.

Richards, J.A., Jia, X., 2006. Remote Sensing Digital Image Analysis. Springer-Verlag, Berlin.

Roberts, D.A., Gardner, M., Church, R., Ustin, S., Scheer, G., Green, R.O., 1998. Mapping Chaparral in the Santa Monica Mountains using Multiple Endmember Spectral Mixture Models. Remote Sens. Env. 65, 267–279.

Sabol, D.E., Adams, J.B., Smith, M.O., 1992. Quantitative subpixel spectral detection of targets in multispectral images. J. Geophy. Res. 97(E2), 2659–2672.

Settle, J., 2005. On the residual term in the linear mixture model and its dependence on the point spread function. IEEE Trans. Geosci. Remote Sens. 43, 398–401.

Settle, J., 2006. On the effect of variable endmember spectra in the linear mixture model. IEEE Trans. Geosci. Remote Sens. 44 (2), 389–396.

Settle, J.J., Drake, N.A., 1993. Linear mixing and the estimation of ground cover proportions. Int. J. Remote Sens. 14, 1159–1177.

Shimabukuro, Y.E., Smith, A.J., 1991. The least-squares mixing models to generate fraction images derived from remote sensing multispectral data. IEEE Trans. Geosci. Remote Sens. 29 (1), 16–20.

Small, C., 2005. A global analysis of urban reflectance. Int. J. Remote Sens. 26, 661–681.

Somers, B., Delalieux, S., Stuckens, J., Verstraeten, W.W., Coppin, P., 2009a. A weighted linear spectral mixture analysis approach to address endmember variability in agricultural production systems. Int. J. Remote Sens. 30, 139–147.

Somers, B., Delalieux, S., Verstraeten, W.W., Verbesselt, J., Lhermitte, S., Coppin, P., 2009b. Magnitude and shape related feature integration in hyperspectral mixture analysis to monitor weeds in citrus orchards. IEEE Trans. Geosci. Remote Sens. 47, 3630–3642.

Somers, B., Delalieux, S., Verstraeten, W.W., van Aardt, J.A.N., Albrigo, G., Coppin, P., 2010a. An automated waveband selection technique for optimized hyperspectral mixture analysis. Int. J. Remote Sens. 31, 5549–5568.

Somers, B., Verbesselt, J., Ampe, E.M., Sims, N., Verstraeten, W.W., Coppin, P., 2010b. Spectral mixture analysis to monitor defoliation in mixed aged Eucalyptus globules Labill plantations in southern Australia using Landsat 5TM and EO-1 Hyperion data. Int. J Appl. Earth Obs. Geoinf. 12, 270–277.

Somers, B., Asner, G.P., Tits, L., Coppin, P., 2011. Endmember variability in spectral mixture analysis: a review. Remote Sens. Env. 115, 1603–1616.

Song, C., 2005. Spectral mixture analysis for subpixel vegetation fractions in the urban environment: How to incorporate endmember variability? Remote Sens. Env. 95, 248–263.

Song, C., Woodcock, C.E., 2003. Estimating tree crown size from multiresolution remotely sensed imagery. Photogramm. Eng. Remote Sens. 69 (11), 1263–1270.

Townshend, J.R.G., Justice, C.O., Gurney, C., McManus, J., 1992. The impact of misregistration on change detection. IEEE Trans. Geosci. Remote Sens. 30 (5), 1054–1060.

Townshend, J.R.G., Huang, C., Kalluri, S.N.V., DeFries, R.S., Liang, S., Yang, K., 2000. Beware of per-pixel characterisation of land cover. Int. J. Remote Sens. 21, 839–843.

Winter, M.E., 1999. N-Findr: an algorithm for fast autonomous spectral end-member determination in hyperspectral data. Proceedings of the SPIE: Imaging Spectrometry 3753, 266–275.

Winter, M.E., Winter, E.M., 2000. Comparison of approaches for determining end-members in hyperspectral data. IEEE Trans. Geosci. Remote Sens. 3, 305–313.

Wu, C., 2004. Normalized spectral mixture analysis for monitoring urban composition using ETM+ imagery. Remote Sens. Env. 93, 480–492.

Xian, G., Crane, M., 2005. Assessments of urban growth in the Tampa Bay watershed using remote sensing data. Remote Sens. Env. 97, 203–215.

Yang, X., Lo, C.P., 2002. Using a time series of satellite imagery to detect land use and land cover changes in the Atlanta, Georgia metropolitan area. Int. J. Remote Sens. 23 (9), 1775–1798.

Yang, F., Matsushita, B., Fukushima, T., 2010. A pre-screened and normalised multiple endmember spectral mixture analysis for mapping impervious surface area in Lake Kasumigaura Basin, Japan. ISPRS J. Photogramm. Remote Sens. 65, 479–490.

Zhang, J., Rivard, B., Sanchez-Azofeifa, A., 2004. Derivative spectral unmixing of hyperspectral data applied to mixtures of lichen and rock. IEEE Trans. Geosci. Remote Sens. 42, 1934–1940.

Zhang, J., Rivard, B., Sanchez-Azofeifa, A., Castro-Esau, K., 2006. Intra- and inter-class spectral variability of tropical tree species at La Selva, Costa Rica: Implications for species identification using HYDICE imagery. Remote Sens. Env. 105, 129–141.

Zheng, M., Cai, Q., Wang, Z., 2005. Effect of prior probabilities on maximum likelihood classifier. Geoscience and Remote Sensing Symposium, 2005, IGARS'05, Proceedings 2005 IEEE International 6, 3753–3756.